



Sub-nanometric Pt clusters supported Co aerogel electrocatalyst with hierarchical micro/nano-porous structure for hydrogen evolution reaction



Tiantian Wang^a, Dan Zhang^c, Jiawei Fei^a, Wenhao Yu^a, Jiawei Zhu^{a,d}, Yanyun Zhang^a, Yue Shi^a, Minge Tian^e, Jianping Lai^{a,*}, Lei Wang^{a,b,**}

^a State Key Laboratory Base of Eco-Chemical Engineering, Ministry of Education, International Science and Technology Cooperation Base of Eco-chemical Engineering and Green Manufacturing, College of Chemistry and Molecular Engineering, Qingdao University of Science and Technology, Qingdao 266042, PR China

^b Shandong Engineering Research Center for Marine Environment Corrosion and Safety Protection, College of Environment and Safety Engineering, Qingdao University of Science and Technology, Qingdao 266042, PR China

^c Key Laboratory of Catalytic Conversion and Clean Energy in Universities of Shandong Province, School of Chemistry and Chemical Engineering, Qufu Normal University, Qufu, Shandong 273165, PR China

^d College of Chemical Engineering, Qingdao University of Science and Technology, Qingdao 266042, PR China

^e Scientific Green (Shandong) Environmental Technology Co., Ltd, Jining Economic Development Zone, Shandong, PR China

ARTICLE INFO

Keywords:

Sub-nanometric clusters
Mass transport
Hierarchical micro/nano-porous
High-current PEM electrolyser
Hydrogen evolution reaction

ABSTRACT

The construction of interactions and synergies between sub-nanometric clusters and supports provides unexpected opportunity to realize high performance and low-cost composite catalysis. However, hierarchical micro/nano-porous structured catalysts closely related to mass transport have been neglected as support, which may play a leading role in industrial practical applications. Herein, we report sub-nanometric Pt clusters supported Co aerogel (Pt_x/Co , X is the wt% of Pt) with hierarchical micro/nano-porous structure, and after optimization of the loading, $Pt_{0.25}/Co$ shows excellent HER performance. Additionally, $Pt_{0.25}/Co$ demonstrates the industrially needed current density of 1.0 A cm^{-2} at 1.8 V in PEM electrolyser, achieving stability in excess of 200 h. Theoretical calculations show that the advantages of the hierarchical micro/nano-porous structure accelerate the mass transport at the three-phase interface, and the strong interaction between sub-nanometric Pt clusters and Co aerogel not only optimizes the electronic structure of $Pt_{0.25}/Co$, but also inhibits the dissolution of sub-nanometric Pt clusters.

1. Introduction

Sub-nanometric clusters (SNCs), with sizes between single atoms and nanoparticles, have become a hot topic of research in the field of catalysis [1–3]. SNCs exhibit unconventional physical and chemical characteristics, mainly including unique electronic structures, higher metal utilization efficiency, and unsaturated coordination environment. These distinguishing characteristics display considerable promise in conventional thermocatalytic reactions, as well as in the rapidly developing electrocatalytic and photocatalytic reactions of recent years [1, 3–6]. This broad variety of applications relies on the development of controlled and precise synthesis methods for different SNCs [7–9].

In general, two parameters primarily govern the triphase (reactants in liquid phase, electron and catalyst in solid phase, products in gas phase) catalytic activity of SNCs: (1) the intrinsic activity of SNCs, and (2) the transport rate of the relevant mass during the catalytic reaction [10–13]. In the past few years, numerous studies have been devoted to the preparation of different SNCs by various strategies, including template-directed, one-step hydrothermal and molten salt-assisted pyrolysis [14–16]. The majority of the already reported methods for the synthesis of SNCs have concentrated on two issues: one is to precisely tune the electronic structure of SNCs, and the other is to regulate the support of SNCs. Both strategies are important to improve the catalytic performance. Hierarchical micro/nano-porous structured catalysts with

* Corresponding author.

** Corresponding author at: State Key Laboratory Base of Eco-Chemical Engineering, Ministry of Education, International Science and Technology Cooperation Base of Eco-chemical Engineering and Green Manufacturing, College of Chemistry and Molecular Engineering, Qingdao University of Science and Technology, Qingdao 266042, PR China.

E-mail addresses: jplai@qust.edu.cn (J. Lai), inorchemwl@126.com (L. Wang).

superhydrophilic/superaerophobic properties can efficiently facilitate mass transport at the three-phase interface [17], yet are overlooked, especially under practical operating conditions. As a result, we envision designing an SNCs catalyst with hierarchical micro/nano-porous structure that emphasises the enhancement of the intrinsic activity while speeding up mass transport at the three-phase interface during the reaction, which can synergistically achieve catalytic performance at high current density.

Herein, we reported sub-nanometric Pt clusters supported Co aerogel (Pt_x/Co , X is the wt% of Pt) with hierarchical micro/nano-porous structure, showing outstanding hydrogen evolution reaction (HER) performance in high-current proton exchange membrane (PEM) electrolyser. Among the first-row-transition metal elements, the metal Co is relatively inexpensive, has satisfactory stability and has the higher surface energy than Pt, making it easier for Pt to support on Co surface [18]. Moreover, the 3d electron orbital of Co metal has a strong interaction with the 5d electron orbital of Pt metal and matching of the lattice parameters between Pt and Co, making it more conducive to electron coupling [19,20]. A series of characterizations indicate that sub-nanometric Pt clusters are successfully supported on the surface of Co aerogel. When the Pt loading is only 0.25% (denoted as: $\text{Pt}_{0.25}/\text{Co}$), it showed excellent electrocatalytic HER performance in 0.5 M H_2SO_4 . $\text{Pt}_{0.25}/\text{Co}$ has the lower overpotential (23 mV at 10 mA cm^{-2} , 111 mV at 500 mA cm^{-2} , 139 mV at 1000 mA cm^{-2}). The turnover frequency (TOF) value reaches 63 s^{-1} at 0.1 V, the charge transfer resistance (R_{CT}) is only 0.8Ω at 500 mA cm^{-2} . Moreover, the $\text{Pt}_{0.25}/\text{Co}$ catalyst, which serves as the cathode in the PEM electrolyser, is just $0.0125 \text{ mg}_{\text{Pt}} \text{ cm}^{-2}$, demonstrating excellent cell voltage (1.59 V at 500 mA cm^{-2} , 1.81 V at 1 A cm^{-2}) and stability (at 500 mA cm^{-2} over 200 h). X-ray photoelectron spectroscopy (XPS) spectra and density functional theory (DFT) calculations reveal that strong electron transport from Co to Pt alters the density of the electron cloud surrounding Pt. The sub-nanometric Pt clusters act as active sites, optimizing the adsorption of H^* for HER process. These excellent properties derived from the advantages of the integrated hierarchical micro/nano-porous structure accelerate the mass transport at the three-phase interface, and the strong interaction between sub-nanometric Pt clusters and Co aerogel not only optimizes the electronic structure of $\text{Pt}_{0.25}/\text{Co}$, but also inhibits the coalescence, detachment and dissolution of sub-nanometric Pt clusters.

2. Experimental section

2.1. Materials

Cobalt nitrate hexahydrate ($\text{Co}(\text{NO}_3)_2 \cdot 6 \text{ H}_2\text{O}$, 99%, Macklin), Chloroplatinic acid hexahydrate ($\text{H}_2\text{PtCl}_6 \cdot 6 \text{ H}_2\text{O}$, Pt \geq 37.5%, Macklin), Glycine ($\text{C}_2\text{H}_5\text{NO}_2$, 98.5%, Sigma-Aldrich), Palladium chloride (PdCl_2 , Pd content 59–60%, Aladdin), Ruthenium chloride anhydrous (RuCl_3 , Ru content 45–55%, Aladdin), Ketjen Black (KB, ECP-600JD) was bought from LION Co, Sulfuric acid (H_2SO_4 , 98%) was purchased from Aladdin. Nafion solution (5%) was purchase from Sigma-Aldrich. The deionized water in the experiment is always ultrapure water (18.2 M Ω -cm).

2.2. Synthesis of $\text{Pt}_{0.25}/\text{Co}$ aerogel

First, under the condition that the metal ion concentration is 0.1 mol L $^{-1}$, stoichiometric amounts of $\text{Co}(\text{NO}_3)_2 \cdot 6 \text{ H}_2\text{O}$ and $\text{H}_2\text{PtCl}_6 \cdot 6 \text{ H}_2\text{O}$ were dissolved in 10 mL of deionized water and glycine was added to the above solution with a molar ratio for metal salt to glycine of 0.6. After stirring, the resulting homogeneous solution was heated to 200 °C in an oil bath, allowing the water to evaporate, forming a thick gel until spontaneous combustion to give a dark brown fluffy powder. Finally, the obtained powder was reduced for 2 h at 700 °C, 5% H_2 + 95% Ar atmosphere with a heating rate of 5 °C/min $^{-1}$.

2.3. Synthesis of Co aerogel

A certain amount of $\text{Co}(\text{NO}_3)_2 \cdot 6 \text{ H}_2\text{O}$ was dissolved in a certain amount of deionized water under the condition that the metal ion concentration was 0.1 mol L $^{-1}$, and the molar ratio of $\text{Co}(\text{NO}_3)_2 \cdot 6 \text{ H}_2\text{O}$ to glycine was kept at 0.6. The subsequent synthesis procedures are the same as that of $\text{Pt}_{0.25}/\text{Co}$ aerogel.

2.4. Synthesis of other aerogels

The synthesis methods of other aerogels are similar to the synthesis method of $\text{Pt}_{0.25}/\text{Co}$ aerogel. The difference is that the addition amounts of the two metals and glycine are different, but the ion concentration is 0.1 mol L $^{-1}$, the molar ratio of metal salt to glycine was both 0.6.

2.5. Characterizations

Scanning electron microscopy (SEM) images were obtained by Hitachi, S-8200. The transmission electron microscope (TEM) and high-resolution TEM (HRTEM) of the catalyst were tested using FEI Tecnai-G2 F30 at an accelerating voltage of 80 KV. Powder X-ray diffraction (XRD) spectra were recorded on an X'Pert-Pro MPD diffractometer with Cu K α radiation at 40 KV and 40 mA. XPS analysis was performed with an Axis Supra spectrometer using a monochromatic Al K α source at 15 mA and 14 kV. The composition of as-prepared samples was collected by the inductively coupled plasma-atomic emission spectroscopy (ICP-AES, Agilent 8800). The catalysts after the durability test were sonicated in ethanol and then collected for the next step of characterization.

2.6. Electrochemical tests

On the CHI 760 electrochemical workstation (Shanghai Chenhua Instrument Co., Ltd., China), the traditional three electrode system was used for the test, with Ag/AgCl as the reference electrode, carbon rod as the counter electrode, and glass carbon electrode (GCE, diameter: 3 mm, area: 0.07065 cm 2) as the working electrode. Disperse different catalysts in anhydrous ethanol + 5% Nafion (v: v=1:0.05), and conduct ultrasonic treatment for 1 h to obtain a uniform catalyst ink with a concentration of 1 mg/mL. Then, add 10 μL of the above dispersed liquid drops onto the GCE surface for electrochemical testing. All potentials mentioned below are based on reversible hydrogen electrode (RHE). The formula for potential conversion is $E(\text{RHE}) = E(\text{Ag/AgCl}) + 0.197 \text{ V} + 0.059 \times \text{pH}$. The HER tests were carried out in 0.5 M H_2SO_4 solution. Linear sweep voltammetry (LSV) was used to test the HER activity of the catalyst with a scan rate of 5 mV s $^{-1}$ and the corrected iR compensation level is 95%. Electrochemical impedance spectroscopy (EIS) was measured in the frequency range of 10 kHz to 0.01 Hz.

The electrochemical active areas (ECAs) of catalysts were calculated by integrating the CO adsorption areas from the CO-stripping curves, and the charge density for the monolayer adsorption of CO was assumed as $420 \mu\text{C cm}^{-2}$. For CO stripping measurements, CO gas (99.99%) was bubbled into the electrolyte for 15 min while the potential of the working electrode was held at a constant potential of 0.1 V vs. RHE for 900 s. Then, N₂ gas was purged for 15 min to remove CO gas from the electrolyte. After that, CO stripping curves were recorded between 0 and 1.2 V vs. RHE at a scan rate of 20 mV s $^{-1}$.

The turnover frequency (TOF) was calculated by copper underpotential deposition (Cu-UPD) method following the standard equation: $\text{TOF}(\text{s}^{-1}) = \frac{I}{2 \times F \times n}$, $n = \frac{Q_{\text{Cu}}}{2 \times F}$. In the formula, the coefficient 1/2 is based on the assumption that the formation of two electrons on the hydrogen molecule is necessary. I is the current (A) during linear scanning voltammetry (LSV), F is the Faraday constant (96,485.3 C mol $^{-1}$) and n is the number of active sites (mol). The number of active sites (n) were measured by Cu-UPD method. The details are as follows: A new CV at a sweep rate of 50 mV s $^{-1}$ over a range of 0–0.8 V is scanned to obtain a

background curve for correcting the charge associated with any background processes in nitrogen-saturated 0.5 M H₂SO₄ solution. Then, a rated voltage is applied to the working electrode for 100 s to form the Cu-UPD monolayer in 0.5 M H₂SO₄ containing 5.0 mM CuSO₄. The Cu-UPD stripping voltammograms are obtained by sweeping the working electrode voltage from 0.23 to 0.3 V at a sweep rate of 50 mV s⁻¹.

Determination of Faraday efficiency and H₂ generation rate: Pt_{0.25}/Co (cathode) and IrO₂ (anode) catalysts with 0.5 mg cm⁻² were coated on 1 × 1 carbon papers to form a cell, and the volume of H₂ produced can be determined by recording the change in the graduated cylinder reading every 100 s at 0.1 V. Faraday efficiency (FE%) = $\frac{V_A}{V_T} \times 100\%$, where V_A is the actual H₂ volume collected and V_T is the theoretically expected H₂ volume. The H₂ generation rate (HGR) as follows: HGR = $\frac{V_{H2O}}{t \text{ (min)} \times m} \text{ (mL/g)}$, where V_{H2O} is the volume of drained water, m is the total mass of the catalyst, and t is the total reaction time in minutes.

2.7. Preparation of PEM electrolyser

For the assembly of the PEM electrolyser, Nafion®-117 (Dupont) membrane was first treated with 5% H₂O₂ at 80 °C for 1 h; then 5% H₂SO₄ is boiled at 80 °C for 1 h; finally, soak in deionized water for half an hour and rinse repeatedly to remove all kinds of impurities on the surface. A uniform catalyst ink was prepared by mixing Pt_{0.25}/Co and IrO₂ with 5 wt% Nafion solution and ethanol, respectively. Then, Pt_{0.25}/Co (cathode) and IrO₂ (anode) inks were sprayed on both sides of the Nafion®-117 membrane in an ultrasonic spraying system to prepare the catalyst-coated membrane (CCM). The metal loadings of the cathode and anode were 0.5 mg cm⁻² and 2 mg cm⁻², respectively. Ti felt was used as the anode gas diffusion layer (GDL), and carbon paper was used as the anode GDL. The CCM was sandwiched between the two diffusion layers and hot-pressed at 140 °C, 5 MPa to form a membrane-electrode assembly (MEA) with an effective area of 1.0 cm⁻². The prepared MEA was placed between two bipolar plates (BP), and a single channel snake-shaped flow field was used in the BP to facilitate the flow of reactants and products. Finally, use nuts and bolts to tighten the two PEM electrolyser units.

2.8. Density functional theory (DFT) calculations

We have employed the first-principles to perform density functional theory (DFT) calculations within the generalized gradient approximation (GGA) using the Perdew-Burke-Ernzerhof (PBE) formulation. We have chosen the projected augmented wave (PAW) potentials to describe the ionic cores and take valence electrons into account using a plane wave basis set with a kinetic energy cutoff of 450 eV. Partial occupancies of the Kohn–Sham orbitals were allowed using the Gaussian smearing method and a width of 0.05 eV. The electronic energy was considered self-consistent when the energy change was smaller than 10–6 eV. A geometry optimization was considered convergent when the energy change was smaller than 0.03 eV Å⁻¹. The vacuum spacing in a direction perpendicular to the plane of the structure is 18 Å for the surfaces. A DFT-D correction with Grimme scheme was used to account for the dispersion interaction. The U correction is set as 4.65 eV for Co atoms. The Brillouin zone integration is performed using 2 × 2 × 1 Monkhorst-Pack k-point sampling for a structure. Finally, the adsorption energies (E_{ads}) were calculated as E_{ads} = E_{ad/sub} - E_{ad} - E_{sub}, where E_{ad/sub}, E_{ad}, and E_{sub} are the total energies of the optimized adsorbate/substrate system, the adsorbate in the structure, and the clean substrate, respectively. The free energy was calculated using the equation:

$$G = E_{ads} + ZPE - TS$$

where G, E_{ads}, ZPE and TS are the free energy, total energy from DFT calculations, zero point energy and entropic contributions, respectively.

3. Results and discussion

3.1. Synthesis and characterizations of Pt_{0.25}/Co catalyst

In this paper, sub-nanometric Pt clusters supported Co aerogels with hierarchical micro/nano-porous structure were synthesized by auto-combustion method and subsequent reduction procedure [21,22]. In this method, beaker containing the metal precursors and the glycine solution were placed in an oil bath, followed by evaporation of solvent and spontaneous combustion of products at 200 °C, metal oxide with porous structure was formed (Fig. S1). Then, Pt_{0.25}/Co (the loading amount of Pt is 0.25%) was formed after high-temperature reduction at 700 °C for 2 h (Fig. S2). Compared with the traditional drying and sol-gel methods, the auto-combustion and subsequent reduction procedure method has the following advantages: Firstly, during spontaneous combustion of the solution, the expanding gas forms a spongy or foamy microstructure. This microstructure can be controlled by adjusting the precursor concentration. When the hot gas escapes from the sample, it carries away a large amount of heat, and the solid product cools faster with smaller particles and higher porosity. In addition, by controlling the reduction temperature, nano-sized powders with the desired crystal structure can be fabricated. Finally, the auto-combustion method uses water as the solvent and the reaction is simple and fast, which can usually be completed in a few minutes. To compare the effect of sub-nanometric Pt clusters supported aerogel, pure Co aerogel was prepared using the same method.

X-ray diffraction (XRD) pattern of Pt_{0.25}/Co is similar to the Co aerogel (Fig. 1a). Among them, the peaks of 44.21°, 51.52°, 75.85° correspond to the (111), (200), (220) crystal planes of Co (JCPDS No. 15–0806), and appear as phase face-centered cubic (fcc) structure. No corresponding Pt peaks were discovered because of the exceedingly low Pt concentration. Compared to Co aerogel, Pt_{0.25}/Co can still keep its original porosity and morphology, according to images from scanning electron microscopy (SEM) and transmission electron microscopy (TEM) (Fig. 1b, Fig. S3 and S4a-b). Fig. S4c shows that aerogel is a three-dimensional network array composed of interconnected network nanowires. In addition, the corresponding high angle annular dark-field STEM (HAADF-STEM) image reveals small bright spots uniformly dispersed on the catalyst surface (marked with yellow circles), demonstrating the majority of Pt in the form of clusters with average size of 1.6 nm (Fig. 1c). The high-resolution TEM (HRTEM) image shows that the lattice spacing of the catalyst is 0.208 nm, mainly exposing the (111) crystal plane of Co (Fig. 1d). In addition, high-density bright spots (red circle markers) are observed on the lattice surface, which can be reasonably distributed to sub-nanometric Pt clusters. The magnified image of the region shows that Co atoms are dispersed around Pt atoms (different contrast points in Fig. 1e), indicating that there may be an interaction between Pt and Co. Due to the different radii and heights of the two atoms, the line intensity extracted from Fig. 1f clearly indicates that the brighter point is indeed Pt atoms (Fig. 1g). TEM-mapping (Fig. 1h) and SEM-mapping (Fig. S4d-f) show the existence of Co and Pt elements, as well as their homogeneous distribution over the entire area measured. This series of characterization proved the successful synthesis of Pt_{0.25}/Co. The surface area of Pt_{0.25}/Co was analyzed by N₂ physical adsorption isotherms (Fig. S5a). According to the brunauer-emmett-teller (BET) model, the surface area was 23.8 m² g⁻¹ and the inset shows that it mainly existed mesopores (2–50 nm). In addition, as shown in Fig. S5b, Pt_{0.25}/Co could be compressed from ≈ 0.7–0.1 cm (14% of its original height), and then the morphology is basically recovered after being immersed in water for 5 s, indicating its good scalability. To demonstrate the reproducibility of the auto-combustion method in terms of structure, the Pt_{0.25}/Co catalyst was synthesized three times. As shown in Fig. S5c-e, all three SEM images have similar structures, proving the reproducibility of the catalyst synthesized by this method.

To explore the valence state and electronic environment of the

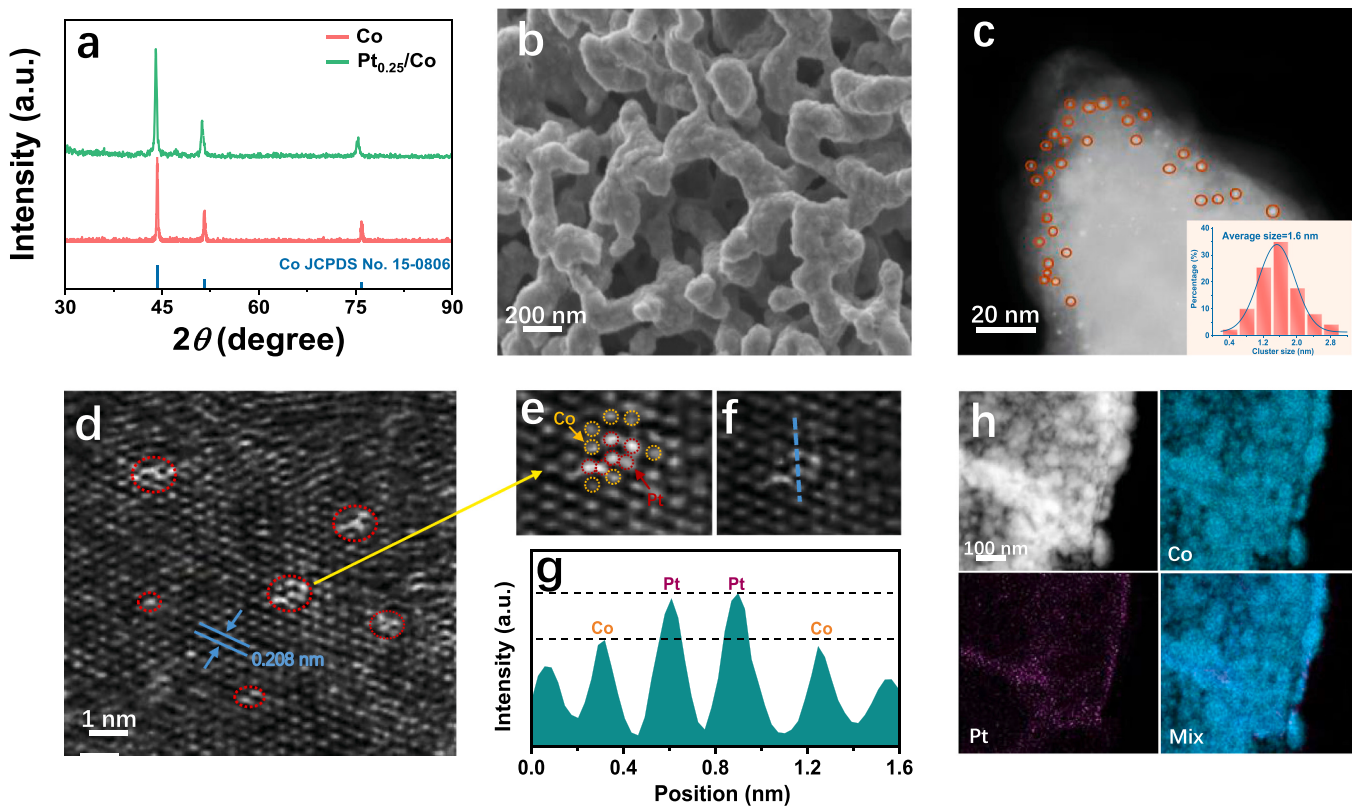


Fig. 1. (a) The XRD pattern of $\text{Pt}_{0.25}/\text{Co}$. (b) SEM image of $\text{Pt}_{0.25}/\text{Co}$. (c) HAADF-STEM image of $\text{Pt}_{0.25}/\text{Co}$ (insert: size distribution). (d-f) Magnified HRTEM image of $\text{Pt}_{0.25}/\text{Co}$. (g) The extracted line intensity along with the blue direction. (h) TEM image and corresponding elemental mapping image of $\text{Pt}_{0.25}/\text{Co}$.

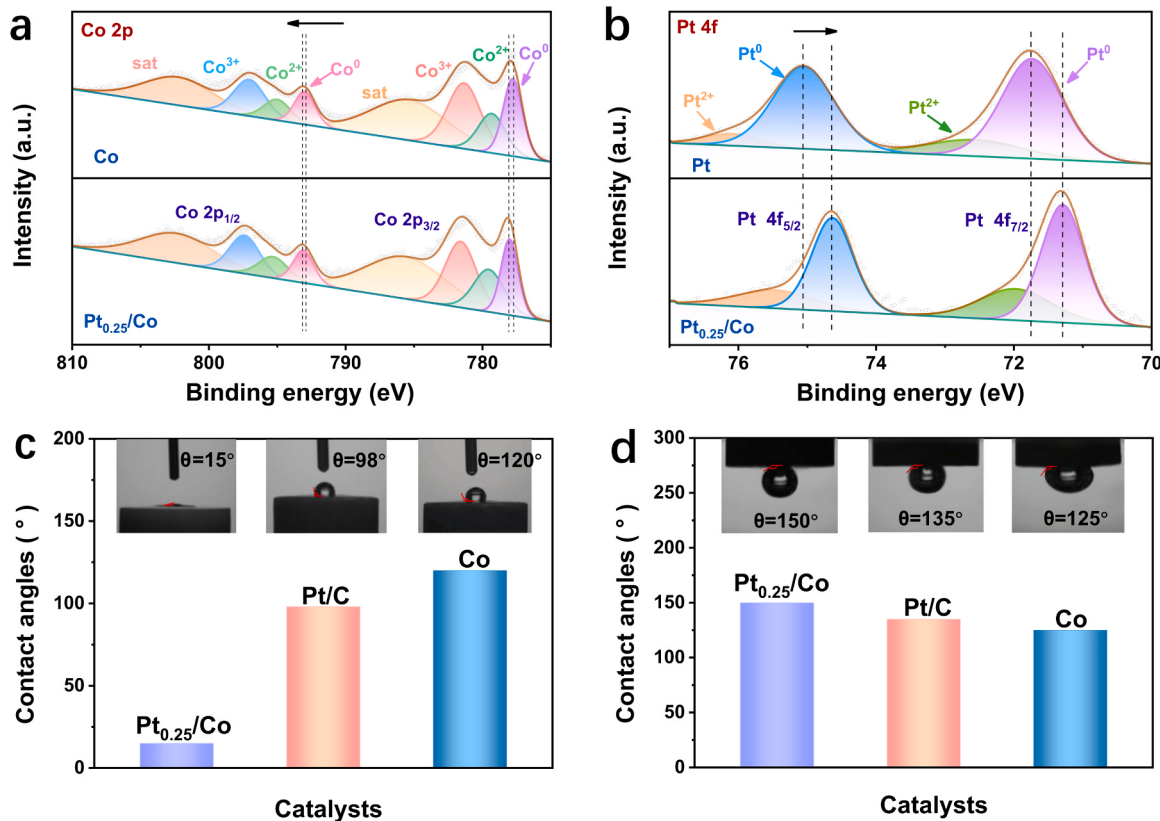


Fig. 2. (a) High resolution XPS spectra of Co 2p of Co aerogel and $\text{Pt}_{0.25}/\text{Co}$. (b) High resolution XPS spectra of Pt 4 f spectra of Co aerogel and $\text{Pt}_{0.25}/\text{Co}$. (c) Contact angles of $\text{Pt}_{0.25}/\text{Co}$, Pt/C and Co. (d) Bubble contact angles of $\text{Pt}_{0.25}/\text{Co}$, Pt/C and Co.

Pt_{0.25}/Co, XPS was employed for characterization. As shown in Fig. 2a, the peaks at 777.8 eV and 793.0 eV for the Co aerogel are attributed to Co⁰ 2p_{3/2} and Co⁰ 2p_{1/2}, respectively [23,24]. In addition, the peaks at 779.3 eV and 795 eV are derived from Co²⁺ [25,26], the peaks at 781.3 eV and 797.1 eV are derived from Co³⁺ [27], the partial oxidation state may be caused by prolonged exposure to air [28,29]. Fig. 2b shows that the characteristic peaks at 71.7 eV and 75.0 eV are derived from Pt⁰ 4 f_{7/2} and Pt⁰ 4 f_{5/2} [30], and the peaks at 72.8 eV and 76.1 eV are attributed to Pt²⁺ [31]. It can be concluded from the position of the aforementioned binding energy that the positive shift of Co 2p peak is estimated to be around 0.2 eV and the negative shift of Pt 4f peak is estimated to be about 0.4 eV after Pt loading. This further proves that the loading of Pt results in the charge transfer from Co to Pt. Co aerogels as electron donors enrich the electron density of Pt and further enhance the metal-support interaction.

In addition, the superhydrophilicity and superaerophobicity of the catalyst are extremely crucial for accelerating the HER reaction kinetics. Because the continuous and violent bubbles generated during the HER process at high current density adhere to the catalyst surface will

increase the charge and proton transport resistance at the interface, which is detrimental to enhancing HER activity [17,32]. As shown in Fig. 2c, the contact angle of Pt_{0.25}/Co is 15°, which is considerably less than that of Pt/C (98°) and pure Co (120°). The results show that Pt_{0.25}/Co exhibits ultra-high hydrophilicity, which facilitates close contact between the electrolyte and the electrode. Moreover, the bubble performance test is illustrated in Fig. 2d, compared with Pt/C (135°) and (125°), the bubble contact angle of Pt_{0.25}/Co is 150°, indicating that Pt_{0.25}/Co has superaerophobicity, which can accelerate the release of hydrogen bubbles from the electrode surface and facilitate the continuous exposure of active sites.

By changing the mass ratio of Co(NO₃)₂•6 H₂O and H₂PtCl₆•6 H₂O, we synthesized Co aerogels with different Pt loading amounts by the same method, namely Pt_{0.14}/Co aerogel, Pt_{0.18}/Co aerogel, Pt_{0.32}/Co aerogel. All of the prepared aerogels displayed a comparable three-dimensional porous morphology, judging by SEM images (Fig. S6). With the increase of Pt loading amounts, the Pt particles became larger, the number of agglomerated groups increased, and the aerogel porosity decreased. All catalysts were quantitatively analyzed by inductively

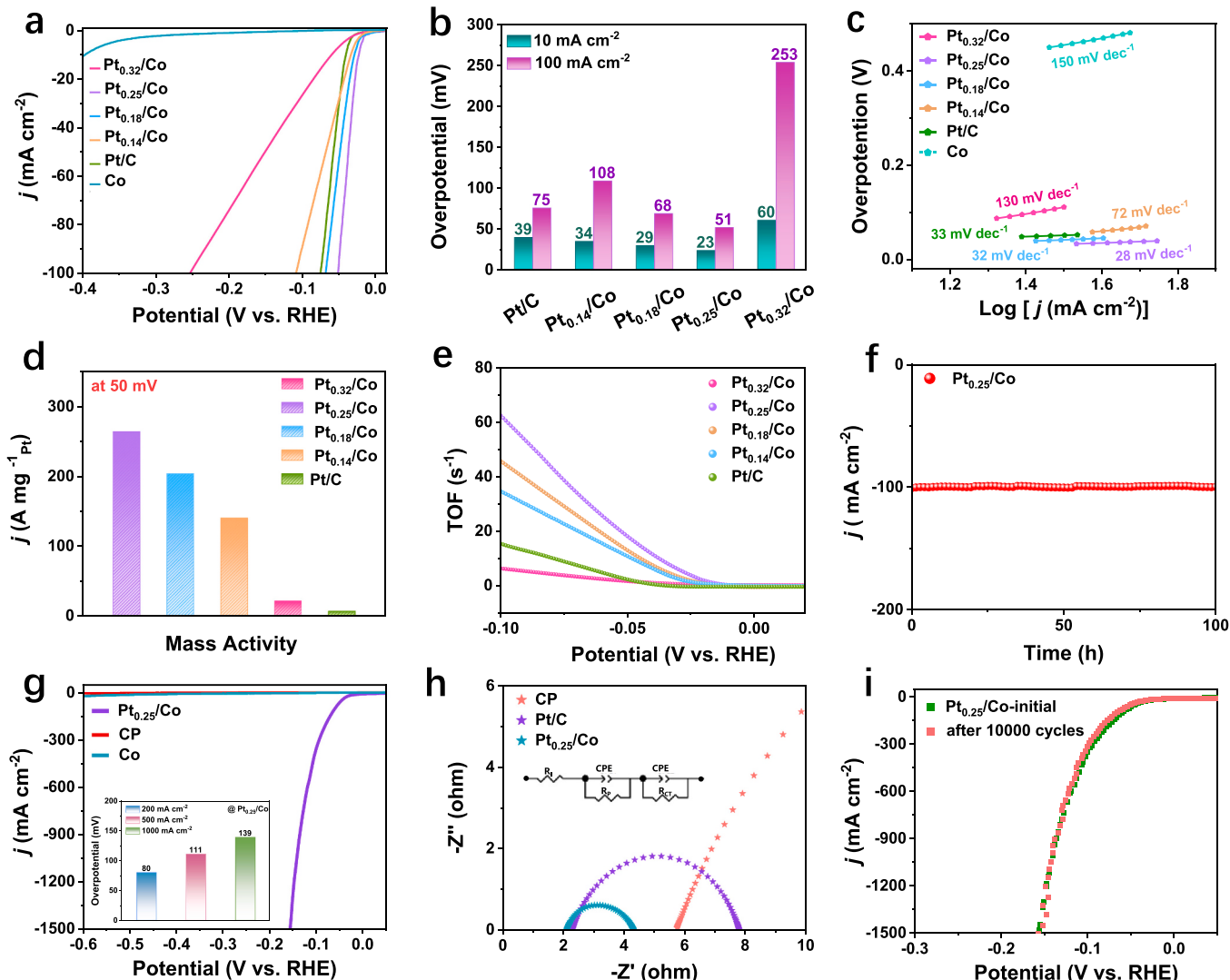


Fig. 3. (a) HER polarization curves of Pt_{0.32}/Co, Pt_{0.25}/Co, Pt_{0.18}/Co, Pt_{0.14}/Co, Pt/C and Co catalysts in N₂-saturated 0.5 M H₂SO₄ solution. (b) Comparison of overpotential at 10 mA cm⁻². (c) Tafel plots obtained from the polarization curves in a. (d) Mass activities of different electrocatalysts at -0.05 V vs. RHE. (e) TOF values of Pt_{0.32}/Co, Pt_{0.25}/Co, Pt_{0.18}/Co, Pt_{0.14}/Co, and Pt/C. (f) i-t curve of Pt_{0.25}/Co for 100 h. (g) Polarization curves of Pt_{0.25}/Co, CP and Co in 0.5 M H₂SO₄ solution (insert: Comparison of overpotential at 200 mA cm⁻², 500 mA cm⁻², 1000 mA cm⁻²). (h) Nyquist plots of Pt_{0.25}/Co, Pt/C and CP. (Inset: The electrical equivalent circuit used for fitting EIS, where R_i and R_{CT} denote the intrinsic electrode and electrolyte resistance and the charge transfer resistance, respectively, R_p is the pore resistance, CPEs represent the constant phase elements). (i) Polarization curves for Pt_{0.25}/Co initial and after 10000 CV cycles.

coupled plasma atomic emission spectrometer (ICP-AES). The corresponding data are in Table S1. Next, the XRD patterns of the three catalysts were analyzed, showing that all the diffraction peaks were the fcc structure of Co (Fig. S7). Fig. S8 lists the XPS spectra of the three catalysts, it can be seen that these catalysts exhibit the same electron transfer trend as Pt_{0.25}/Co. It is further proved that Pt is catalytic active centers with abundant electrons.

3.2. Electrocatalytic performance tests toward HER

In order to explore the influence of sub-nanometric Pt clusters supported, we tested the HER performance in a N₂-saturated 0.5 M H₂SO₄ electrolyte using a three-electrode system. Fig. 3a shows the linear sweep voltammetry (LSV) curves of Pt_{0.14}/Co aerogel, Pt_{0.18}/Co aerogel, Pt_{0.25}/Co aerogel, Pt_{0.32}/Co aerogel, Co aerogel and 20% commercial Pt/C. Specifically, the overpotential of Pt_{0.25}/Co at 10 mA cm⁻² is merely 23 mV, which is lower than that of Pt_{0.14}/Co aerogel (34 mV), Pt_{0.18}/Co aerogel (29 mV), Pt_{0.32}/Co aerogel (60 mV) and commercial Pt/C (39 mV). This also reflects that the Co aerogel has virtually no HER activity, and the catalysts' active ingredients do indeed originate from supported sub-nanometric Pt clusters. Similarly, Pt_{0.25}/Co still exhibits the lowest overpotential (51 mV) at a current density of 100 mA cm⁻² (Fig. 3b). As shown in Fig. 3c, the Tafel slope of Pt_{0.25}/Co is only 28 mV dec⁻¹, which indicates that the rate determining step is the recombination of adsorbed hydrogen, following the Volmer-Tafel mechanism [33–35]. The quick kinetics of the hydrogen generation reaction are revealed by the tiny value of Tafel slope, which is advantageous for practical application [36–38]. Generally speaking, the electrochemical active area (ECSA) is proportional to the double layer capacitance (C_{dl}) of the catalyst [39–41]. C_{dl} was measured by cyclic voltammetry (CV) tests at different scan rates (Fig. S9a–e), the results show that the C_{dl} of Pt_{0.25}/Co is 4.86 mF cm⁻², which is higher than that of Pt_{0.14}/Co aerogel (3.06 mF cm⁻²), Pt_{0.18}/Co aerogel (3.68 mF cm⁻²), Pt_{0.32}/Co aerogel (2.25 mF cm⁻²) and Co aerogel (1.13 mF cm⁻²) (Fig. S9f). In addition, the ECSAs of the prepared catalysts were further determined by CO stripping experiment at 0.5 M H₂SO₄ (Fig. S10), and the ECSA of Pt_{0.25}/Co was estimated to be 152.4 m² g⁻¹, larger than Pt_{0.14}/Co (92.2 m² g⁻¹), Pt_{0.18}/Co (124.1 m² g⁻¹), Pt_{0.32}/Co (81.44 m² g⁻¹) and Pt/C (75.6 m² g⁻¹). The above directly demonstrates that Pt_{0.25}/Co has a largest ECSA, offering more active sites to increase HER activity. Fig. S11 depicts Pt loading normalized mass activities at different potentials. At –0.05 V vs. RHE, the mass activity of Pt_{0.25}/Co reached 263.5 A mg_{Pt}⁻¹, which is 43.8 times higher than that of Pt/C (6.2 A mg_{Pt}⁻¹) (Fig. 3d). As is well-known, turnover frequency (TOF) is one of the important indicators to evaluate the intrinsic activity of catalysts [42–44]. Based on the quantity of active sites obtained using Cu underpotential deposition (Cu-UPD) [29] (Fig. S12–13), the TOF value of Pt_{0.25}/Co reaches 63 s⁻¹ at 0.1 V (Fig. 3e), which is far ahead of the reported Pt-based catalysts (Table S2). This indicates that appropriate amount of Pt loading can effectively enhance the intrinsic activity of the catalyst. In addition, catalytic stability is another indispensable parameter to evaluate the catalytic effect of catalysts [45–47]. Subsequent long-term current-time (i-t) tests demonstrated that the Pt_{0.25}/Co could be maintained at high current for at least 100 h (Fig. 3f), demonstrating excellent long-time durability. The Faraday efficiency of Pt_{0.25}/Co for HER was determined from the H₂ produced by the drainage method. Fig. S14a shows the change in the measuring cylinder. We plotted Faraday curves based on the data collected. As shown in Fig. S14b, by comparing the measured and calculated values of H₂ production, the Faraday efficiency of Pt_{0.25}/Co is close to 98.7%, reflecting the high selectivity to H₂. When the cell was operated for 1000 s, 12.6 mL of H₂ was produced, from which the H₂ generation rate was calculated to be about 1511.7 mL min⁻¹ g⁻¹.

To adjust to industrial production, it is required to investigate the activity and stability of catalysts under high current density [48]. The optimal catalyst Pt_{0.25}/Co was evenly spread on carbon paper (CP), and

the HER performance under high current density was tested in 0.5 M H₂SO₄. As shown in Fig. 3g, the onset potential of the Pt_{0.25}/Co is very small, and when the current density reaches 200 mA cm⁻², 500 mA cm⁻² and 1000 mA cm⁻², the overpotentials are only 80 mV and 111 mV and 139 mV. Electrochemical impedance spectroscopy (EIS) measurements were carried out in the frequency range of 100, 000–0.01 Hz at 500 mA cm⁻² to confirm the electron transfer rate and mass transport rate of HER at high current density. Fig. 3h shows the Nyquist diagram of CP, Pt/C and Pt_{0.25}/Co at 100 mV. In the medium to low-frequency region of their EIS spectra, two characteristic semicircles of distinguishing diameters can be seen, which corresponding to different pore resistances (R_p) and charge transfer resistances (R_{CT}) in parallel with the constant phase elements (CPEs). At high frequencies, the intercepts on the real axis indicate the intrinsic resistance (R_I) of the electrolyte and the electrode. Based on the equivalent circuit of these generic descriptors (inset in Fig. 3h), the R_{CT}, R_p, and R_I values of the micro/nano-porous Pt_{0.25}/Co are as low as 1.4 Ω, 0.8 Ω and 2.1 Ω, respectively, indicating Pt_{0.25}/Co have superior reaction kinetics and mass transport kinetics, in sharp contrast with Pt/C values (3.9 Ω, 1.6 Ω, 2.3 Ω). The LSV before and after 10,000 CV cycling hardly suffered any weakening (Fig. 3i), demonstrating the excellent catalytic stability of the Pt_{0.25}/Co at the high current density. The content of Pt in the catalyst was determined by ICP-AES. The measurement result was 0.23%, which was similar to the initial catalyst content. The XRD pattern shows that the Pt_{0.25}/Co still maintains the Co fcc crystal phase (Fig. S15a). As indicated by SEM and HAADF-STEM images, the morphology of the aerogel remains well (Fig. S15b–c). In conclusion, the Pt_{0.25}/Co is demonstrated remarkable structural stability under high current density. This is due to the fact that the introduction of sub-nanometric Pt clusters makes Pt_{0.25}/Co form integrated hierarchical micro/nano-porous structure to ensure its superhydrophilicity and superhydrophobicity, which is conducive to the mass transport of H⁺ at the three-phase interface, reducing the resistance of charge and keeping a stable environment of electroactive site. Moreover, the strong binding force between Pt and Co effectively inhibits the coalescence, detachment and dissolution of sub-nanometric Pt clusters, sequentially improving the overall stability of the catalyst.

Similarly, to investigate the impact of structural modifications on alkaline HER performance, additional tests were conducted using a typical three-electrode setup in an N₂-saturated 1 M KOH electrolyte. Fig. S16a indicates that Pt_{0.25}/Co achieved the best HER catalytic activity among the catalysts studied in 1.0 M KOH solution, with an overpotential of 33 mV at the current density of 10 mA cm⁻² (Fig. S16b), which is much lower than the overpotentials of Pt_{0.14}/Co (75 mV), Pt_{0.18}/Co (52 mV), Pt_{0.32}/Co (117 mV) and commercial Pt/C (37 mV). Besides, the Tafel slope of 47.8 mV dec⁻¹ for Pt_{0.25}/Co was significantly lower than that of Pt/C (48.6 mV dec⁻¹) and different loadings of catalysts, indicating that the fast HER kinetic was based on the Volmer-Heyrovsky mechanism under alkaline condition [49] (Fig. S16c). We summarized dozens of recently reported excellent alkaline HER electrocatalysts for activity comparison (Table S3), and the results showed that Pt_{0.25}/Co exhibited good performance among the reported electrocatalysts. As shown in Fig. S16d, after Pt mass normalization at different potentials, Pt_{0.25}/Co still exhibited the most excellent mass activity (116.9 A mg_{Pt}⁻¹) at –0.05 V vs. RHE. The TOF value of Pt_{0.25}/Co peaked at 8 s⁻¹ at 0.1 V vs. RHE., surpassing the other prepared catalysts (Fig. S16e). The activity of the electrode remained essentially unchanged for 80 h when continuously testing at 10 mA cm⁻² (Fig. S16f). Moreover, we tested the HER performance at high current density. Fig. S16g shows that the overpotentials of Pt_{0.25}/Co were 167 mV, 270 mV, and 461 mV at current densities up to 100 mA cm⁻², 200 mA cm⁻², and 500 mA cm⁻². EIS plots at –0.3 Vs. RHE revealed that Pt_{0.25}/Co demonstrated the least HER charge transfer resistance (7.6 Ω) compared to other electrocatalysts (Fig. S16h), signifying that this sample displayed rapid reaction kinetics. Fig. S16i presents the polarization curves before and after 10,000 CV cycles,

whereby the decay is insignificant, indicating that the synthesized Pt_{0.25}/Co catalyst also exhibited excellent HER cycling stability under alkaline conditions. The Faraday efficiency of Pt_{0.25}/Co was close to 97.6%, indicating that it had excellent H₂-evolution efficiency (Fig. S17).

3.3. Universal synthesis, characterizations and HER performance tests

To demonstrate the effectiveness and generality of this synthesis method, we further extend the synthesis method to other sub-nanometric noble metal clusters supported Co aerogels, denoted as Ru_{0.25}/Co aerogel, Pd_{0.25}/Co aerogel, respectively. Their XRD patterns characterization (Fig. S18) still only has the fcc crystal phase of Co aerogel, SEM images (Fig. S19a-b, d-e) reveal that both catalysts exhibited similar three-dimensional porous morphologies, and HAADF-STEM images (Fig. S19c, f) display that Ru clusters and Pd clusters are uniformly dispersed on the catalyst surface. Additionally, XPS spectra show that Ru_{0.25}/Co aerogel and Pd_{0.25}/Co aerogel also show the same electron transfer trend as Pt_{0.25}/Co, which proves that Ru and Pd are active centers with abundant electrons (Fig. S20). Meanwhile, the series of catalysts still have superior HER activity and stability than Co aerogel in 0.5 M H₂SO₄ (Fig. S21-S25).

3.4. DFT calculation analysis

DFT calculation was employed for the theoretical analysis in order to better understand the mechanism of HER activity augmentation caused by the introduction of sub-nanometric Pt clusters supported. Schematic model of Pt_{0.25}/Co and Pt/C adsorption of H are shown in Fig. 4a-b. HER is a multi-step process, in which the first step is hydrogen adsorption ($H^+ + e^- \rightarrow H^*$), the subsequent step is the release of molecular hydrogen, following the Tafel ($2H^* \rightarrow H_2$) or Heyrovsky ($H^* + H^+ + e^- \rightarrow H_2$) mechanism [50,51]. Therefore, the optimal hydrogen adsorption free energy (ΔG_{H^*}) should be close to zero to ensure the dynamic balance between proton capture and hydrogen release [52]. It can be seen from the ΔG_{H^*} diagram (Fig. 4c), compared with Pt/C (-0.12 eV), the ΔG_{H^*} of Pt_{0.25}/Co is -0.06 eV, indicating that Pt_{0.25}/Co has hydrogen adsorption

free energy closer to 0 eV and higher HER activity. We speculate that the enhanced HER activity of Pt_{0.25}/Co is closely related to the strongest interaction between Pt and Co. Therefore, differential charge density analysis of Pt_{0.25}/Co was carried out. As shown in Fig. 4d, the region of charge concentration enhancement is caused by the strong dipole polarization of Pt and Co at the interface. The interfacial electron transfer from Co to Pt makes it easy to obtain electrons on the surface of Pt, resulting in a significant quantity of negative charge on Pt. It also indicates that the strong metal-support electron interaction at the interface improves the catalytic performance, which is consistent with XPS description.

3.5. PEM electrolyser performance

PEM water electrolysis is regarded as the optimum technique for producing H₂ from renewable energy due to its high gas purity, superior proton conductivity, low gas crossover, and higher current density [53–55]. Because of the significant HER activity and stability of Pt_{0.25}/Co catalyst in the three-electrode system, we further evaluated the practical application potential of Pt_{0.25}/Co with a loading of 0.5 mg cm⁻² in water electrolysis in the PEM electrolyser at 50 °C. The PEM electrolyser model is depicted in Fig. 5a. The cathode and anode catalysts are Pt_{0.25}/Co and IrO₂ supported on carbon paper, respectively. IrO₂ was chosen because of its well-known high durability and activity in oxygen evolution reaction. As shown in Fig. 5b, the polarization curves indicated that Pt_{0.25}/Co || IrO₂ had a smaller cell voltage (1.69 V) at 1 A cm⁻² for water electrolysis activity, significantly preceding to the commercial Pt/C || IrO₂ (1.76 V). In addition, we also carried out chronopotentiometry tests on Pt_{0.25}/Co || IrO₂ to evaluate the long-term operation stability of PEM electrolyser. Fig. 5c shows that the voltage of Pt_{0.25}/Co || IrO₂ is almost unchanged after running 200 h at the current density of 1 A cm⁻².

In addition, we performed EIS tests on PEM electrolyser using Pt_{0.25}/Co and Pt/C as cathode electrocatalysts, respectively (Fig. S26a). The EIS curves were further fitted by an equivalent circuit model (Fig. S26a, inset). R_{cell} denotes the cell ohmic resistance, which is related to the ohmic losses of all components, R_{ac} denotes the activation resistance to

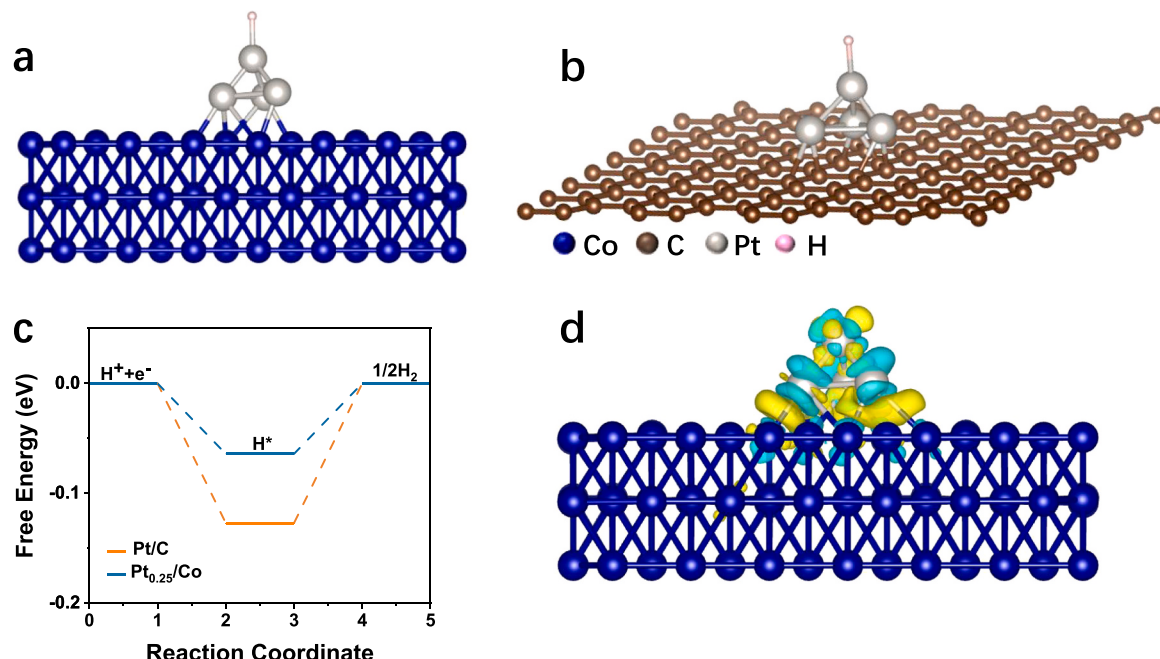


Fig. 4. (a) and Pt/C (b) adsorption of H. (c) Pt/C and Pt_{0.25}/Co hydrogen adsorption free energy (ΔG_{H^*}). (d) Differential charge density of Pt_{0.25}/Co. The yellow and blue isosurfaces represent charge accumulation and depletion in space, and the isosurface energy level is 0.01 eV/Å³. The blue, silver, brown and pink spheres represent the Co, Pt, C and H atoms, respectively.

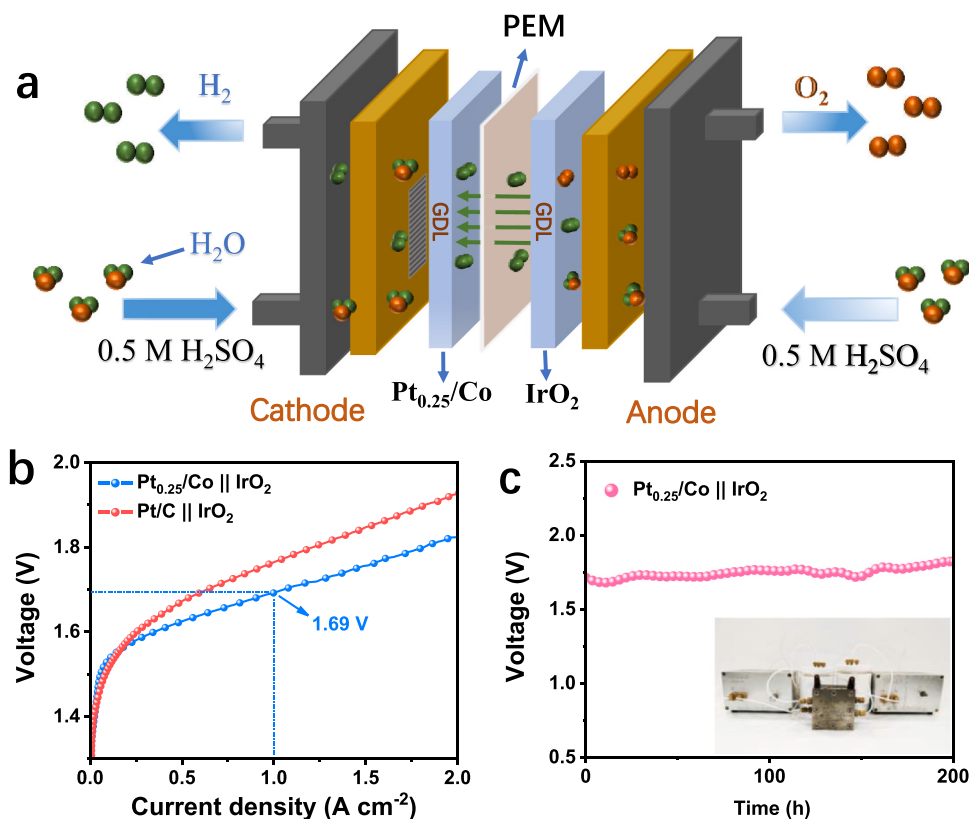


Fig. 5. (a) Schematic diagram of PEM electrolyser. (b) Polarization curves of the PEM electrolyser with Pt_{0.25}/Co and commercial Pt/C as cathode catalyst and IrO₂ as anode catalyst at 50 °C. (c) Chronopotentiometry curve for PEM electrolyser running at 500 A cm⁻² with Pt_{0.25}/Co as cathode and IrO₂ as anode catalyst. The inset shows a photo of the PEM electrolyser.

determine the reaction kinetics of the anode and cathode electrocatalysts, and R_d denotes the resistance to mass transport as reflected by the Warburg diffusion element (W_d). As seen in Fig. S26b, Pt_{0.25}/Co has lower mass transport resistance and cell ohmic resistance compared to Pt/C, further indicating that the Pt_{0.25}/Co electrodes in the PEM electrolyser will reduce ohmic losses and mass transport losses. These excellent properties clearly demonstrate the great potential of the Pt_{0.25}/Co catalyst in practical applications.

4. Conclusion

In summary, we reported sub-nanometric Pt clusters with hierarchical micro/nano-porous structure supported aerogel by using Co aerogel as metal support to optimize mass transport for HER in PEM electrolyser. A series of characterizations indicate that sub-nanometric Pt clusters are successfully supported on the surface of Co aerogel. Pt_{0.25}/Co showed the best HER performance when the Pt loading was only 0.25%. In addition, X-ray photoelectron spectroscopy (XPS) and density functional theory (DFT) calculations reveal that the strong electron transport from Co to Pt changes the electron cloud density around Pt, thereby optimizing the adsorption of H*. These excellent properties derived from the advantages of the catalyst structure, including the integrative metallic backbone is beneficial to reduce the electrochemical impedance to achieve rapid electron transfer, and the introduction of sub-nanometric Pt clusters makes Pt_{0.25}/Co form integrated hierarchical micro/nano-porous aerogel structure to ensure its superhydrophilicity /superaerophobicity, which is conducive to the mass transport at the three-phase interface. In addition, the strong interaction between Pt and Co aerogels not only optimizes the electronic structure of Pt_{0.25}/Co, but also inhibits the coalescence, detachment and dissolution of sub-nanometric Pt clusters, thereby enhancing the activity and stability of the electrocatalyst. Unexpectedly, this method can also

be used to synthesize low sub-nanometric Ru/Pd clusters supported Co aerogels. This work provides valuable contributions and inspiration for the future design of sub-nanometric metal clusters catalyst with hierarchical micro/nano-porous structure with potential application value.

CRediT authorship contribution statement

L.W. and J.L. supervised the research. J.L. conceived the research. T.W. and D.Z. designed the experiments. T.W. performed most of the experiments and data analysis. J.F., W.Y. and J.Z prepared the electrodes and helped with electrochemical measurements. Y.Z., Y.S and M.T. helped analyze physical characterization data. All authors discussed the results and commented on the manuscript.

Declaration of Competing Interest

The authors declare that they have no known competing financial interests or personal relationships that could have appeared to influence the work reported in this paper.

Data Availability

The authors do not have permission to share data.

Acknowledgements

This work was supported by the National Natural Science Foundation of China (52272222, 52072197), Youth Innovation and Technology Foundation of Shandong Higher Education Institutions, China (2019KJC004), Outstanding Youth Foundation of Shandong Province, China (ZR2019JQ14), Taishan Scholar Young Talent Program (tsqn201909114, tsqn201909123), Natural Science Foundation of

Shandong Province (ZR2020YQ34), Major Scientific and Technological Innovation Project (2019JZZY020405), and Major Basic Research Program of Natural Science Foundation of Shandong Province under Grant (ZR2020ZD09).

Appendix A. Supporting information

Supplementary data associated with this article can be found in the online version at [doi:10.1016/j.apcatb.2023.123546](https://doi.org/10.1016/j.apcatb.2023.123546).

References

- [1] Q. Hu, K. Gao, X. Wang, H. Zheng, J. Cao, L. Mi, Q. Huo, H. Yang, J. Liu, C. He, Subnanometric Ru clusters with upshifted d band center improve performance for alkaline hydrogen evolution reaction, *Nat. Commun.* 13 (2022), 3958, <https://doi.org/10.1038/s41467-022-31660-2>.
- [2] Y. Tang, X. Jia, Y. Guo, Z. Geng, C. Wang, L. Liu, J. Zhang, W. Guo, X. Tan, T. Yu, J. Ye, Surface unsaturated sulfur modulates Pt sub-nanoparticles on tandem homojunction CdS for efficient electron extraction, *Adv. Energy Mater.* 13 (2023), 2203827, <https://doi.org/10.1002/aenm.202203827>.
- [3] Y. Lu, W. Chen, Sub-nanometre sized metal clusters: From synthetic challenges to the unique property discoveries, *Chem. Soc. Rev.* 41 (2012) 3594–3623, <https://doi.org/10.1039/c2cs1532d>.
- [4] Y. Pi, Z. Qiu, Y. Sun, H. Ishii, Y.F. Liao, X. Zhang, H.Y. Chen, H. Pang, Synergistic mechanism of sub-nanometric Ru clusters anchored on tungsten oxide nanowires for high-efficient bifunctional hydrogen electrocatalysis, *Sci. Adv.* 10 (2023), e2206096, <https://doi.org/10.1002/adv.202206096>.
- [5] R. Zhao, Y. Wang, G. Ji, J. Zhong, F. Zhang, M. Chen, S. Tong, P. Wang, Z. Wu, B. Han, Z. Liu, Partially nitrided Ni nanoclusters achieve energy-efficient electrocatalytic CO₂ reduction to CO at ultralow overpotential, *Adv. Mater.* 35 (2023), e2205262, <https://doi.org/10.1002/adma.202205262>.
- [6] Z. Jia, X. Qin, Y. Chen, X. Cai, Z. Gao, M. Peng, F. Huang, D. Xiao, X. Wen, N. Wang, Z. Jiang, W. Zhou, H. Liu, D. Ma, Fully-exposed Pt–Fe cluster for efficient preferential oxidation of CO towards hydrogen purification, *Nat. Commun.* 13 (2022), 6798, <https://doi.org/10.1038/s41467-022-34674-y>.
- [7] J. Liu, W. Shi, X. Wang, Cluster-nuclei assembled into two-dimensional hybrid CuO-PMA sub-1 nm nanosheets, *J. Am. Chem. Soc.* 141 (2019) 18754–18758, <https://doi.org/10.1021/jacs.9b08818>.
- [8] L. Wang, J. Diao, M. Peng, Y. Chen, X. Cai, Y. Deng, F. Huang, X. Qin, D. Xiao, Z. Jiang, N. Wang, T. Sun, X. Wen, H. Liu, D. Ma, Cooperative sites in fully exposed Pd clusters for low-temperature direct dehydrogenation reaction, *ACS Catal.* 11 (2021) 11469–11477, <https://doi.org/10.1021/acscatal.1c01503>.
- [9] F. Meng, M. Peng, Y. Chen, X. Cai, F. Huang, L. Yang, X. Liu, T. Li, X. Wen, N. Wang, D. Xiao, H. Jiang, L. Xia, H. Liu, D. Ma, Defect-rich graphene stabilized atomically dispersed Cu₃ clusters with enhanced oxidase-like activity for antibacterial applications, *Appl. Catal., B* 301 (2022), 120826, <https://doi.org/10.1016/j.apcatb.2021.120826>.
- [10] Z. Li, M. Di, W. Wei, L. Leng, Z. Li, C. He, Q. Tan, Q. Xu, J.H. Horton, L. Li, J. Zhu, Alkali ion-promoted palladium subnanoclusters stabilized on porous alumina nanosheets with enhanced catalytic activity for benzene oxidation, *Nano Res.* 15 (2022) 5912–5921, <https://doi.org/10.1007/s12274-022-4250-5>.
- [11] Q. Sun, N. Wang, Q. Bing, R. Si, J. Liu, R. Bai, P. Zhang, M. Jia, J. Yu, Subnanometric hybrid Pd-M(OH)₂, M= Ni, Co, clusters in zeolites as highly efficient nanocatalysts for hydrogen generation, *Chem* 3 (2017) 477–493, <https://doi.org/10.1016/j.chempr.2017.07.001>.
- [12] Z. Liu, Y. Du, R. Yu, M. Zheng, R. Hu, J. Wu, Y. Xia, Z. Zhuang, D. Wang, Tuning mass transport in electrocatalysis down to sub-5 nm through nanoscale grade separation, *Angew. Chem. Int. Ed.* 62 (2023), e202212653, <https://doi.org/10.1002/anie.202212653>.
- [13] R. Zhang, Z. Liu, S. Zheng, L. Wang, L. Zhang, Z.A. Qiao, Pyridinic nitrogen sites dominated coordinative engineering of subnanometric Pd clusters for efficient alkynes' semidihydrogenation, *Adv. Mater.* 35 (2023), e2209635, <https://doi.org/10.1002/adma.202209635>.
- [14] X. Zhao, X. Kong, F. Wang, R. Fang, Y. Li, Metal sub-nanoclusters confined within hierarchical porous carbons with high oxidation activity, *Angew. Chem. Int. Ed.* 65 (2021) 10842–10849, <https://doi.org/10.1002/anie.202016591>.
- [15] Y. Tian, H. Duan, B. Zhang, S. Gong, Z. Lu, L. Dai, C. Qiao, G. Liu, Y. Zhao, Template guiding for the encapsulation of uniformly subnanometric platinum clusters in beta-zeolites enabling high catalytic activity and stability, *Angew. Chem. Int. Ed.* 60 (2021) 21713–21717, <https://doi.org/10.1002/anie.202108059>.
- [16] Q. Sun, B.W.J. Chen, N. Wang, Q. He, A. Chang, C.M. Yang, H. Asakura, T. Tanaka, M.J. Hulsey, C.H. Wang, J. Yu, N. Yan, Zeolite-encaged Pd-mn nanocatalysts for CO₂ hydrogenation and formic acid dehydrogenation, *Angew. Chem. Int. Ed.* 59 (2020) 20183–20191, <https://doi.org/10.1002/anie.202008962>.
- [17] L. Wen, X. Shan, J. Liu, H. Mu, Y. Xiao, B. Mei, W. Liu, G. Lin, Z. Jiang, L. Jiang, Engineered superhydrophilic/superaerophobic electrocatalysts composed of supported CoMoS_x chalcogels for overall water splitting, *Angew. Chem. Int. Ed.* 59 (2019) 1659–1665, <https://doi.org/10.1002/anie.201911617>.
- [18] L.Z. Mezey, J. Giber, The surface free energies of solid chemical elements: Calculation from internal free enthalpies of atomization, *Jpn. J. Appl. Phys.* 21 (1982) 1569–1571, <https://doi.org/10.1143/jjap.21.1569>.
- [19] J. Li, S. Sharma, X. Liu, Y.-T. Pan, J.S. Spendelow, M. Chi, Y. Jia, P. Zhang, D. A. Cullen, Z. Xi, H. Lin, Z. Yin, B. Shen, M. Muzzio, C. Yu, Y.S. Kim, A.A. Peterson, K.L. More, H. Zhu, S. Sun, Hard-magnet L₁-CoPt nanoparticles advance fuel cell catalysis, *Joule* 3 (2018) 124–135, <https://doi.org/10.1016/j.joule.2018.09.016>.
- [20] L. Liang, H. Jin, H. Zhou, B. Liu, C. Hu, D. Chen, Z. Wang, Z. Hu, Y. Zhao, H.-W. Li, D. He, S. Mu, Cobalt single atom site isolated Pt nanoparticles for efficient ORR and HER in acid media, *Nano Energy* 88 (2021), 106221, <https://doi.org/10.1016/j.nanoen.2021.106221>.
- [21] G. Han, M. Li, H. Liu, W. Zhang, L. He, F. Tian, Y. Liu, Y. Yu, W. Yang, S. Guo, Short-range diffusion enables general synthesis of medium-entropy alloy aerogels, *Adv. Mater.* 34 (2022), e2202943, <https://doi.org/10.1002/adma.202202943>.
- [22] A. Varma, A.S. Mukasyan, A.S. Rogachev, K.V. Manukyan, Solution combustion synthesis of nanoscale materials, *Chem. Rev.* 116 (2016) 14493–14586, <https://doi.org/10.1021/acs.chemrev.6b00279>.
- [23] S. Choi, M. Oh, Well-arranged and confined incorporation of PdCo nanoparticles within a hollow and porous metal-organic framework for superior catalytic activity, *Angew. Chem. Int. Ed.* 58 (2019) 866–871, <https://doi.org/10.1002/anie.201812827>.
- [24] Y. Yang, R. Zeng, Y. Xiong, F.J. DiSalvo, H.D. Abruna, Cobalt-based nitride-core oxide-shell oxygen reduction electrocatalysts, *J. Am. Chem. Soc.* 141 (2019) 19241–19245, <https://doi.org/10.1021/jacs.9b10809>.
- [25] T. Chen, Z. Zhang, B. Cheng, R. Chen, Y. Hu, L. Ma, G. Zhu, J. Liu, Z. Jin, Self-templated formation of interlaced carbon nanotubes threaded hollow Co₃S₄ nanoboxes for high-rate and heat-resistant lithium–sulfur batteries, *J. Am. Chem. Soc.* 139 (2017) 12710–12715, <https://doi.org/10.1021/jacs.7b06973>.
- [26] H. Liu, G. Xia, R. Zhang, P. Jiang, J. Chen, Q. Chen, Mof-derived RuO₂/Co₃O₄ heterojunctions as highly efficient bifunctional electrocatalysts for HER and OER in alkaline solutions, *RSC Adv.* 7 (2017) 3686–3694, <https://doi.org/10.1039/c6ra25810g>.
- [27] B.J. Tan, K.J. Klabunde, P.A. Sherwood, Xps studies of solvated metal atom dispersed (smad) catalysts. Evidence for layered cobalt-manganese particles on alumina and silica, *J. Am. Chem. Soc.* 113 (1991) 855–861, <https://doi.org/10.1021/ja00003a019>.
- [28] J. Yu, Y. Guo, S. She, S. Miao, M. Ni, W. Zhou, M. Liu, Z. Shao, Bigger is surprisingly better: agglomerates of larger RuP nanoparticles outperform benchmark Pt nanocatalysts for the hydrogen evolution reaction, *Adv. Mater.* 30 (2018), e1800047, <https://doi.org/10.1002/adma.201800047>.
- [29] X. Wu, Z. Wang, D. Zhang, Y. Qin, M. Wang, Y. Han, T. Zhan, B. Yang, S. Li, J. Lai, L. Wang, Solvent-free microwave synthesis of ultra-small Ru-Mo₂C@CNT with strong metal-support interaction for industrial hydrogen evolution, *Nat. Commun.* 12 (2021), 4018, <https://doi.org/10.1038/s41467-021-24322-2>.
- [30] Q. Cheng, C. Hu, G. Wang, Z. Zou, H. Yang, L. Dai, Carbon-defect-driven electroless deposition of Pt atomic clusters for highly efficient hydrogen evolution, *J. Am. Chem. Soc.* 142 (2020) 5594–5601, <https://doi.org/10.1021/jacs.9b11524>.
- [31] C. Wang, F. Hu, H. Yang, Y. Zhang, H. Lu, Q. Wang, 1.82 wt% Pt/N, P co-doped carbon overwhelms 20 wt% Pt/C as a high-efficiency electrocatalyst for hydrogen evolution reaction, *Nano Res.* 10 (2016) 238–246, <https://doi.org/10.1007/s12274-016-1281-9>.
- [32] Z. Wu, Y. Zhao, H. Wu, Y. Gao, Z. Chen, W. Jin, J. Wang, T. Ma, L. Wang, Corrosion engineering on iron foam toward efficiently electrocatalytic overall water splitting powered by sustainable energy, *Adv. Funct. Mater.* 31 (2021), 2010437, <https://doi.org/10.1002/adfm.202010437>.
- [33] D.H. Kweon, M.S. Okyay, S.J. Kim, J.P. Jeon, H.J. Noh, N. Park, J. Mahmood, J. Baek, Ruthenium anchored on carbon nanotube electrocatalyst for hydrogen production with enhanced faradaic efficiency, *Nat. Commun.* 11 (2020), 1278, <https://doi.org/10.1038/s41467-020-15069-3>.
- [34] I. Hod, P. Deria, W. Bury, J.E. Mondloch, C.W. Kung, M. So, M.D. Sampson, A. W. Peters, C.P. Kubiatk, O.K. Farha, J.T. Hupp, A porous proton-relaying metal-organic framework material that accelerates electrochemical hydrogen evolution, *Nat. Commun.* 6 (2015), 8304, <https://doi.org/10.1038/ncomms9304>.
- [35] Z. Peng, K. Wang, W. Xu, B. Wang, B. Mao, Y. Han, C.-K. Tsung, B. Yang, Z. Liu, Y. Li, Strong interface enhanced hydrogen evolution over molybdenum-based catalysts, *ACS Appl. Energy Mater.* 3 (2020) 5219–5228, <https://doi.org/10.1021/acsaem.0c00045>.
- [36] J. Wang, H. Yang, F. Li, L. Li, J. Wu, S. Liu, T. Cheng, Y. Xu, Q. Shao, X. Huang, Single-site Pt-doped RuO₂ hollow nanospheres with interstitial C for high-performance acidic overall water splitting, *Sci. Adv.* 8 (2022), eab9271, <https://doi.org/10.1126/sciadv.abl9271>.
- [37] Y. Ge, X. Wang, B. Chen, Z. Huang, Z. Shi, B. Huang, J. Liu, G. Wang, Y. Chen, L. Li, S. Lu, Q. Luo, Q. Yun, H. Zhang, Preparation of fcc-2H-fcc heterophase Pd@Ir nanostructures for high-performance electrochemical hydrogen evolution, *Adv. Mater.* 34 (2022), e22017399, <https://doi.org/10.1002/adma.202107399>.
- [38] S.A. Shah, L. Xu, R. Sayyar, I. Khan, A. Yuan, X. Shen, X. Li, H. Ullah, FeNi@N-doped graphene core-shell nanoparticles on carbon matrix coupled with MoS₂ nanosheets as a competent electrocatalyst for efficient hydrogen evolution reaction, *Adv. Mater. Interfaces* 9 (2022), 2201040, <https://doi.org/10.1002/admi.202201040>.
- [39] H.B. Zhang, P.F. An, W. Zhou, B.Y. Guan, P. Zhang, J.C. Dong, X.W. Lou, Dynamic traction of lattice-confined platinum atoms into mesoporous carbon matrix for hydrogen evolution reaction, *Sci. Adv.* 4 (2018), eaao6657, <https://doi.org/10.1126/sciadv.aao6657>.
- [40] A. Mosallanezhad, C. Wei, P. Ahmadian Koudakan, Y. Fang, S. Niu, Z. Bian, B. Liu, T. Huang, H. Pan, G. Wang, Interfacial synergies between single-atomic Pt and CoS for enhancing hydrogen evolution reaction catalysis, *Appl. Catal., B* 315 (2022), 121534, <https://doi.org/10.1016/j.apcatb.2022.121534>.

- [41] S. Sultan, M.H. Diorizky, M. Ha, J.N. Tiwari, H. Choi, N.K. Dang, P. Thangavel, J. H. Lee, H.Y. Jeong, H.S. Shin, Y. Kwon, K.S. Kim, Modulation of Co and Rh single-atoms and nanoparticles for high-performance hydrogen evolution, *J. Mater. Chem. A* 9 (2021) 10326–10334, <https://doi.org/10.1039/d1ta01067k>.
- [42] H. Yang, Y. Ji, Q. Shao, W. Zhu, M. Fang, M. Ma, F. Liao, H. Huang, Y. Zhang, J. Yang, Z. Fan, Y. Li, Y. Liu, M. Shao, Z. Kang, Metastable-phase platinum oxide for clarifying the Pt-O active site for the hydrogen evolution reaction, *Energy Environ. Sci.* 16 (2023) 574–583, <https://doi.org/10.1039/D2EE03351H>.
- [43] J. Tian, J. Chen, J. Liu, Q. Tian, P. Chen, Graphene quantum dot engineered nickel-cobalt phosphide as highly efficient bifunctional catalyst for overall water splitting, *Nano Energy* 48 (2018) 284–291, <https://doi.org/10.1016/j.nanoen.2018.03.063>.
- [44] H. You, D. Wu, D. Si, M. Cao, F. Sun, H. Zhang, H. Wang, T.F. Liu, R. Cao, Monolayer niir-layered double hydroxides as a long-lived efficient oxygen evolution catalyst for seawater splitting, *J. Am. Chem. Soc.* 144 (2022) 9254–9263, <https://doi.org/10.1021/jacs.2c00242>.
- [45] W. Yu, H. Huang, Y. Qin, D. Zhang, Y. Zhang, K. Liu, Y. Zhang, J. Lai, L. Wang, The synergistic effect of pyrrolic-N and pyridinic-N with Pt under strong metal-support interaction to achieve high-performance alkaline hydrogen evolution, *Adv. Energy Mater.* 12 (2022), 2200110, <https://doi.org/10.1002/aenm.202200110>.
- [46] F. Lyu, S. Zeng, Z. Jia, F.X. Ma, L. Sun, L. Cheng, J. Pan, Y. Bao, Z. Mao, Y. Bu, Y. Li, J. Lu, Two-dimensional mineral hydrogel-derived single atoms-anchored heterostructures for ultrastable hydrogen evolution, *Nat. Commun.* 13 (2022), 6249, <https://doi.org/10.1038/s41467-022-33725-8>.
- [47] J. Huo, J.-P. Tessonnier, B.H. Shanks, Improving hydrothermal stability of supported metal catalysts for biomass conversions: a review, *ACS Catal.* 11 (2021) 5248–5270, <https://doi.org/10.1021/acscatal.1c00197>.
- [48] Y. Tan, R. Xie, S. Zhao, X. Lu, L. Liu, F. Zhao, C. Li, H. Jiang, G. Chai, D.J.L. Brett, P. R. Shearing, G. He, I.P. Parkin, Facile fabrication of robust hydrogen evolution electrodes under high current densities via Pt@Cu interactions, *Adv. Funct. Mater.* 31 (2021), 2105579, <https://doi.org/10.1002/adfm.202105579>.
- [49] S. Bai, M. Xie, T. Cheng, K. Cao, Y. Xub, X. Huang, Surface engineering of Rh_{0.05} nanosheets promotes hydrogen evolution in alkaline, *Nano Energy* 78 (2020), 105224, <https://doi.org/10.1016/j.nanoen.2020.105224>.
- [50] Z. Lin, B. Xiao, M. Huang, L. Yan, Z. Wang, Y. Huang, S. Shen, Q. Zhang, L. Gu, W. Zhong, Realizing negatively charged metal atoms through controllable d-electron transfer in ternary Ir_{1-x}Rh_xSb intermetallic alloy for hydrogen evolution reaction, *Adv. Energy Mater.* 12 (2022), 2200855, <https://doi.org/10.1002/aenm.202200855>.
- [51] N.K. Dang, M. Umer, P. Thangavel, S. Sultan, J.N. Tiwari, J.H. Lee, M.G. Kim, K. S. Kim, Surface enrichment of iridium on IrCo alloys for boosting hydrogen production, *J. Mater. Chem. A* 9 (2021) 16898–16905, <https://doi.org/10.1039/d1ta02597j>.
- [52] Z. Pu, J. Zhao, I.S. Aminu, W. Li, M. Wang, D. Heab, S. Mu, A universal synthesis strategy for P-rich noble metal diphosphide-based electrocatalysts for the hydrogen evolution reaction, *Energy Environ. Sci.* 12 (2019) 952–957, <https://doi.org/10.1039/c9ee00197b>.
- [53] T. Reier, H.N. Nong, D. Teschner, R. Schlögl, P. Strasser, Electrocatalytic oxygen evolution reaction in acidic environments-reaction mechanisms and catalysts, *Adv. Energy Mater.* 7 (2017) 1601275, <https://doi.org/10.1002/aenm.201601275>.
- [54] C.V. Pham, M. Bühlert, J. Knöppel, M. Bierling, D. Seeberger, D. Escalera-López, K. J.J. Mayrhofer, S. Cherevko, S. Thiéle, IrO₂ coated TiO₂ core-shell microparticles advance performance of low loading proton exchange membrane water electrolyzers, *Appl. Catal., B* 269 (2020), 118762, <https://doi.org/10.1016/j.apcatb.2020.118762>.
- [55] J. Shan, T. Ling, K. Davey, Y. Zheng, S.Z. Qiao, Transition-metal-doped RuRu bifunctional nanocrystals for overall water splitting in acidic environments, *Adv. Mater.* 31 (2019), e1900510, <https://doi.org/10.1002/adma.201900510>.